3D-Printed Tissue-Mimicking Phantoms for Medical Imaging and Computational Validation Applications

Aidan J. Cloonan,[1–3] Danial Shahmirzadi,[4,5] Ronny X. Li,[4] Barry J. Doyle,[6,7] Elisa E. Konofagou,[4,8] and Tim M. McGloughlin[1,3,9]

Abstract

Abdominal aortic aneurysm (AAA) is a permanent, irreversible dilation of the distal region of the aorta. Recent efforts have focused on improved AAA screening and biomechanics-based failure prediction. Idealized and patient-specific AAA phantoms are often employed to validate numerical models and imaging modalities. To produce such phantoms, the investment casting process is frequently used, reconstructing the 3D vessel geometry from computed tomography patient scans. In this study the alternative use of 3D printing to produce phantoms is investigated. The mechanical properties of flexible 3D-printed materials are benchmarked against proven elastomers. We demonstrate the utility of this process with particular application to the emerging imaging modality of ultrasound-based pulse wave imaging, a noninvasive diagnostic methodology being developed to obtain regional vascular wall stiffness properties, differentiating normal and pathologic tissue in vivo. *Phantom wall displacements under pulsatile loading conditions were observed, showing good correlation to fluid–structure interaction simulations and regions of peak wall stress predicted by finite element analysis. 3D-printed phantoms show a strong potential to improve medical imaging and computational analysis, potentially helping bridge the gap between experimental and clinical diagnostic tools.*

Introduction

Cardiovascular disease is one of the leading causes of death and morbidity in the United States and worldwide, frequently leading to aneurysmal dilation or occlusion of vessel lumens. Abdominal aortic aneurysms (AAAs) account for approximately 15,000 deaths per year in the United States and 1.3% of all deaths among men aged 65–85 worldwide.[1] A majority of clinicians use AAA maximum diameter and growth rate as surgical intervention criteria. The risk of rupture is highest when the aneurysm reaches 5–5.5 cm in diameter, prompting clinical intervention.[2,3] However, it is well known that small aneurysms (<5 cm) may rupture and that larger aneurysms may remain quiescent for years.[4,5] AAA rupture is a dramatic process with associated high mortality rates; thus, immediate clinical intervention is required. Postrupture, approximately 40% of total fatalities occur before hospital admission.[6] After emergency repair of the ruptured AAA, 40–50% of patients die during or within 30 days of operation.[7]

Over the past decade, with modern advances in computational modeling and clinical imaging techniques, it has

[1]Centre for Applied Biomedical Engineering Research, Department of Mechanical, Aeronautical and Biomedical Engineering; [2]Irish Centre for Composites Research, Materials and Surface Science Institute; and [3]Materials and Surface Science Institute, University of Limerick, Limerick, Ireland.
[4]Ultrasound and Elasticity Imaging Laboratory, Department of Biomedical Engineering, and [8]Department of Radiology, Columbia University, New York, New York.
[5]Department of Mechanical Engineering, Stevens Institute of Technology, Hoboken, New Jersey.
[6]Intelligent Systems for Medicine Laboratory, School of Mechanical and Chemical Engineering, University of Western Australia, Perth, Australia.
[7]Centre for Cardiovascular Science, University of Edinburgh, Edinburgh, United Kingdom.
[9]Department of Biomedical Engineering, Khalifa University of Science, Technology & Research, Abu Dhabi, United Arab Emirates.

MARY ANN LIEBERT, INC. • VOL. 1 NO. 1 • 2014 • DOI: 10.1089/3dp.2013.0010

become increasingly clear that patient-specific wall stress calculations outperform the classical maximum diameter interventional criterion. Recent efforts have focused on AAA screening and biomechanics-based failure prediction. Several screening programs have been implemented worldwide for aneurysm detection, generally targeting the demographic at greatest risk, men greater than 65 years old.[8] Screening usually involves the use of cost-effective ultrasonography to detect AAAs with a sensitivity approaching 100%.[9]

Elastomeric vascular anatomic models or phantoms are often employed to validate numerical models and diagnostic imaging modalities. To produce such 3D tissue-mimicking phantoms, the investment casting process is frequently used, reconstructing the AAA geometry from computed tomography (CT) patient scans.[10–13] However, this process is somewhat costly, labor-intensive, and not without its limitations. Several characteristics are desirable for resultant phantoms. At a minimum the phantom must replicate the geometry with a good surface finish. The material should have sufficient strength and durability to withstand physiological pressures, be impermeable to water for flow studies, and possess nonlinear elastomeric properties similar to native aortic tissue. The incorporation of filler particles is useful to mimic the "scattering" properties of tissue when subjected to ultrasonic imaging techniques. Scattering occurs when the passage of the ultrasound beam is reflected in many directions when irregularly shaped particles smaller than the beam wavelength are encountered. Further information on this topic is provided in the article by Hoskins.[14] Finally, transparency or translucency is also useful for medical device deployment and bench testing.

In the current study we investigate the use of 3D printing to produce tissue-mimicking phantoms. The performance of two flexible 3D-printed materials, FullCure TangoPlus FLX930 and HeartPrint Flex, are benchmarked against several poly(dimethylsiloxane) (PDMS) Sylgard elastomers. These include Sylgard 160 (S160), Sylgard 170 (S170), a 50:50 mix of Sylgard 160 and 170 (S160/S170), Sylgard 184 (S184), and Sylgard 184/Agar (S184A). Many of these materials have been previously utilized in the preparation of vascular phantoms.[10,15,16] To further establish the capability of both processing techniques, challenging models of a patient-specific aneurysm and healthy aorta were also sought. We demonstrate the utility of 3D-printed phantoms with particular application to the emerging imaging modality of ultrasound-based pulse wave imaging (PWI). PWI can identify regional vascular wall stiffness properties and differentiate normal and pathologic tissue *in vivo*.[17–23] Fluid–structure interaction (FSI) simulations and finite element analysis are conducted to provide further insight of the phantom response to physiological loading conditions.

Materials and Methods

3D Reconstruction: From 2D Computed Tomography Slices to 3D Geometries

Two types of aortic models were evaluated in this study, designated "idealized" and "patient-specific" models. The idealized model is based on preoperative measurements of AAAs obtained from the Eurostar (EUROpean collaborators on Stent-graft Techniques for abdominal aortic Aneurysm Repair) Data Registry Centre. A total of 3,413 patients were treated in this study, and baseline, procedural, and follow-up results were recorded.[23] For each AAA case, 11 dimensional parameters (e.g., proximal aortic neck, aneurysm sac, and bifurcation angle) were recorded by the clinician, and these were averaged to define the idealized AAA geometry.[24] The lumen diameters of the idealized model are a 50 mm aneurysm sac, a 24 mm proximal neck, and 12 mm iliac arteries, originating below the 60° aortic bifurcation. To create 3D geometry reconstructions, 2D DICOM images were obtained via CT and processed using the commercial software Mimics v10.0 (Materialise). The software utilizes user-defined thresholding and segmentation parameters based on the intensity of the pixels in the original image. Once segmented, the software generates polylines around the segmented regions, to a user-controlled level of smoothing. This same degree of smoothing can be applied to each reconstruction to remove surface artifacts, while maintaining the geometrical integrity of the AAA.[25] As aortic wall thickness is not readily identifiable from CT scans, a uniform wall thickness of 2mm was defined, as per previous approaches. A high-level schematic of the process flow is shown in Figure 1. For a more comprehensive overview of the 3D reconstruction process, see references.[12,16,26]

Polylines created in Mimics were imported as IGES files into ProEngineer Wildfire 3.0 (PTC; Parametric Technology). Surfaces were then recreated along these polylines and split along the centerline to create two mound halves. Tool paths are subsequently generated by the CAD/CAM software package AlphaCam (Licom Ltd.), and mold halves were machined from aluminum blocks. Two mold sets are required per AAA model: an inner mold set to produce the wax model and a larger outer set to produce the elastomer model. Patient-specific models of healthy and diseased aortas were to compare the capability of both manufacturing processes. The patient-specific CT dataset information complied with the guidance of the local research ethics committee and involved no extra participation by the patients.

AAA Model Manufacture via Investment Casting Process

A general overview of the investment casting process is provided. For a more comprehensive overview of the investment casting process, see references.[11,16,26] Each aluminum mold set is cleaned/degreased thoroughly and sprayed with mold release agent. Molten wax (Castylene B581; Remet Corporation) is incrementally poured into the preheated inner mold to create the sacrificial wax pattern. When solidified, the wax pattern is transferred and aligned in the outer mold set. Shaving or trimming is necessary to remove flash at mold lines or other defects. The aortic wall elastomer material is mixed thoroughly and degassed under vacuum to remove air bubbles from the mixing process. The elastomer is loaded into a large 60ml syringe and the mold filled via the inlet

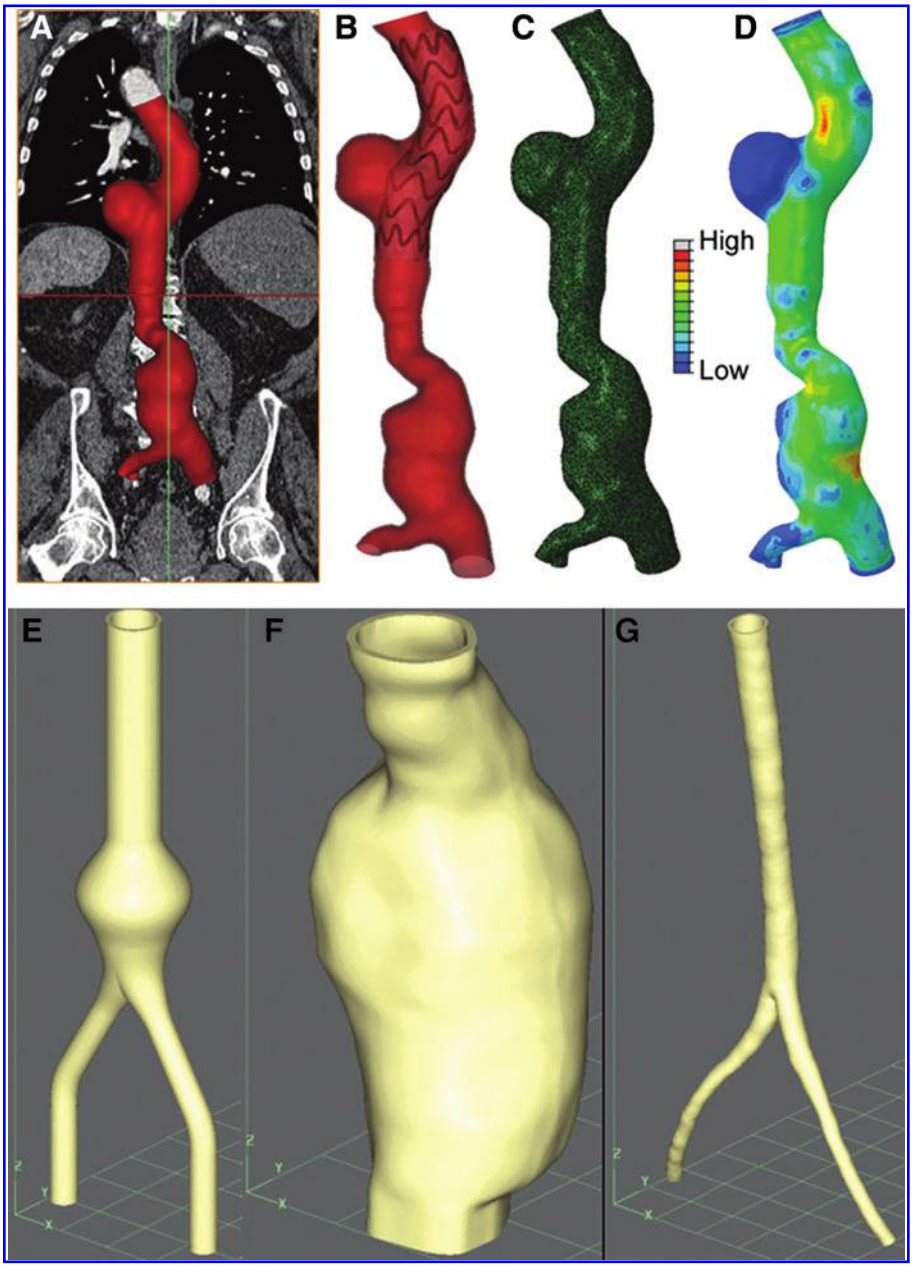

Figure 1. Schematic illustrating the 3D reconstruction process flow. **(A)** A 3D model of the diseased aorta, in this case with upper and lower aneurysms, is created from 2D computed tomography scan images. **(B)** This model may be used for virtual testing of medical devices, such as stent-graft placement. **(C)** The 3D geometry may be subsequently imported into FEA software and meshed and a stress analysis performed **(D)** to determine rupture potential. Phantoms utilized in the current study include a population-averaged idealized aneurysm **(E)**, a patient-specific aneurysm **(F)**, and a healthy aorta **(G)**. Color images available online at www.liebertpub.com/3DP

port(s). The filled outer mold is then transferred to an oven at the recommended curing temperature for several hours. Finally, the model is removed and the wax melted out at 100°C. To create translucent PDMS models with scattering properties similar to tissue, various concentrations of agar were evaluated (data not shown). An optimum concentration of 2.5 wt.% agar (P/N A1296; Sigma-Aldrich) was added to Sylgard 184 and mixed thoroughly to create a new material denoted S184A. All PDMS elastomers were mixed in accordance with the manufacturer's recommendations

AAA Model Manufacture via 3D Printing

Part files were exported from ProEngineer Wildfire 3.0 in Standard Triangulation Language (STL) format and postprocessed with Netfabb Studio Basic v4.9.5 (Netfabb GmbH) to detect and repair STL conversion defects. STL files were viewed in Discover.STL (Redeye; Stratasys Ltd.). Two different photopolymerizable polymers formulated for 3D printing were utilized: TangoPlus FLX930 and HeartPrint Flex, denoted "TP" and "HP," respectively. The TP models were imported to Objet Studio v9 software and printed with an Objet500 Connex 3D printer. This system is capable of printing up to 14 different FullCure materials per job with a layer thickness of 16 μm in high-quality mode. The FullCure materials are acrylic-based photopolymers: FullCure 705 contains unpolymerizable components and was used as support material. The HP models were printed using the HeartPrint 3D printing service by Materialise. This service utilizes a proprietary process and is capable of multimaterial printing.

Uniaxial Tensile Testing

Uniaxial tensile tests were conducted using a Tinius Olsen H25KS (Tinius Olsen Ltd.) screw-driven universal testing machine equipped with roller grips and a 100 N class A loadcell. The extension rate was then set to a constant speed of 500 mm/min as recommended by ISO 37, and strain was evaluated by dividing the stroke reading by the initial measured length of the specimen. Silicone specimens were cast in a dumbbell mold, whereas the 3D-printed materials were cut directly from printed models.

The tensile data were then evaluated in the finite element software Abaqus/CAE (v. 6.11–1; Dassault Systemes), to determine the optimum strain energy function (SEF) and generate hyperelastic material coefficients. The ABAQUS form of the Ogden SEF (Ogden, 1984) takes the form of Equation 1.

$$W(\lambda_1,\lambda_2,\lambda_3)=\sum_{p=1}^{N}\frac{\mu_p}{\alpha_p}(\lambda_1^{\alpha_p},\lambda_2^{\alpha_p},\lambda_3^{\alpha_p}-3) \qquad (1)$$

MARY ANN LIEBERT, INC. • VOL. 1 NO. 1 • 2014 • DOI: 10.1089/3dp.2013.0010

where W is the strain energy density per undeformed unit volume, λ is a principal stretch ratio, α is a strain hardening exponent, and μ is the shear modulus under infinitesimal straining. Ultimate tensile strength (UTS) values and SEF material coefficients are tabulated in Tables 1 and 2, respectively. Population-averaged AAA wall properties are also included for comparison. Raghavan and Vorp[27] modeled the AAA wall as a homogenous, isotropic hyperelastic material, using an SEF taking the form of Equation 2.

$$W = C_1(I_B - 3) + C_2(I_B - 3)^2 \qquad (2)$$

These AAA material properties have been frequently utilized in previous AAA stress analysis studies.[28–30]

Tear Testing

The tear resistance characteristics for each material were evaluated via tear testing. The same experimental apparatus was utilized as for tensile testing. Trouser test pieces as specified by ISO 34–1 method A were tested at a speed of 100mm/min. The characteristic tear strength T_s for each material is given by Equation 3.

$$T_s = \frac{F}{d} \qquad (3)$$

where F and d represent the median force and thickness of the test piece, respectively.

Dynamic Mechanical Analysis

Dynamic mechanical analysis (DMA) was carried out in tension using a Q800 DMA (TA Instruments) equipped with an 18 N loadcell and a thin film clamp. Strips of each material were cut to 4mm width, and the distance between clamps was 15 mm. A multifrequency sweep was then performed up to 50 Hz, with the amplitude (or strain) of oscillation held constant at 10%. The tensile storage modulus (E') represents the elastic stored energy and can be considered equivalent to a stiffness measurement. This frequency range reproduces the typical timescales of periodic motion *in vivo* (peristalsis, skeletal movement, blood flow, etc.). Loading at a high frequency is relevant to the materials viscoelastic response to fast-loading events and is also useful as an accelerated evaluation of the ability of the phantom materials to sustain repeated loading.[31,32]

Topography Analysis

Segments were cut from tubular phantoms to assess the surface topography characteristics. As an inverted microscope is used, specimens were secured to a glass slide with double-sided adhesive tape. Images were captured of the internal surfaces using a Zeiss laser scanning confocal microscope (LSM 710) using a 405 nm laser and a 20×/0.5 NA objective. Image Z-stacks were acquired at an average interval of 1 μm with a pinhole setting of 1 Airy unit (40 μm). Leveling and fitting to a cylindrical profile was performed using

Table 1. Material properties and uniaxial and tear test results for the phantom materials evaluated

Material	Process	Appearance	UTS (MPa)	TS (N/mm)	PWS (MPa)	FEARI
Sylgard 160	LW	Charcoal gray	3.82±0.51[16]	0.49±0.41	0.179	0.05
Sylgard 160/170	LW	Dark gray	3.21±0.38[16]	0.41±0.02	0.185	0.06
Sylgard 170	LW	Black	2.01±0.38[16]	0.32±0.02	0.182	0.09
Sylgard 184	LW	Transparent	7.74±1.66[15]	0.29±0.03	0.172	0.02
Sylgard 184/Agar	LW	Translucent	2.25±0.34	0.49±0.11	0.195	0.09
TangoPlus FLX930	RP	Translucent	2.42±0.46	1.89±0.25	0.188	0.08
HeartPrint Flex	RP	Translucent	0.27±0.03	1.47±0.11	0.258	0.96
AAA tissue	—	Translucent	1.266[36]	—	0.197	0.16

AAA, abdominal aortic aneurysm; FEARI, Finite Element Analysis Rupture Index; PWS, peak wall stress; UTS, ultimate tensile strength; LW, lost wax; RP, rapid prototyping; TS, tear strength.

Table 2. Material coefficients obtained from uniaxial tensile testing

Material	SEF	μ_1	α_1	μ_2	α_2	μ_3	α_3	Reference
Sylgard 160	1st-order Ogden	1.6525	3.2395	—	—	—	—	[16]
Sylgard 160/170	1st-order Ogden	0.5768	2.9278	—	—	—	—	[16]
Sylgard 170	1st-order Ogden	0.6988	2.9741	—	—	—	—	[16]
Sylgard 184	3rd-order Ogden	−304.235	1.2667	148.232	1.5962	157.156	0.9075	[15]
Sylgard 184/Agar	3rd-order Ogden	58.959	−2.959	4.156	6.396	−61.291	−5.164	Current
TangoPlus FLX930	3rd-order Ogden	−0.0116	4.2228	0.003398	5.1519	0.3360	−4.4742	Current
HeartPrint Flex	3rd-order Ogden	0.1703	4.2436	−0.1029	4.8823	0.1214	−5.1206	Current
AAA tissue	Raghavan & Vorp	0.174	—	1.881	—	—	—	[27]

SEF, strain energy function.

the Zen 2008 topography software module (Carl Zeiss MicroImaging GmbH). Validation was carried out using a surface roughness reference specimen (Type 112 1107) with an average arithmetic roughness (Ra) of 5.8μm, as previously described.[31] Finally, a median filter was applied and areal surface texture parameters were processed in accordance with ISO 25178.

Scattering Evaluation

Tubular semi-opaque phantoms were immersed and imaged with a clinical SonixTOUCH ultrasound scanner (Ultrasonix Medical Corporation) with linear probe L14-5/38. This enables a qualitative comparison of the scattering properties for each material. Phantom cross-sectional views are shown in Supplementary Figure S1 (Supplementary Data are available online at www.liebertpub.com/3dp).

Finite Element Analysis

The idealized AAA model geometry, with a 2mm uniformly thick wall, was imported into Abaqus/CAE for stress analysis. The geometry was meshed using 3D 10-node tetrahedral elements (C3D10H), and the experimentally derived material properties were applied for each case. The AAA wall was modeled as a nearly incompressible, homogenous, isotropic hyperelastic material. The idealized model was fully constrained at the proximal neck and distal iliac regions, and a static physiological pressure of 120 mmHg (16kPa) was applied to the inner surface. For each material type, the peak wall stress is computed to derive the Finite Element Analysis Rupture Index (FEARI),[30] given by Equation 4.

$$\text{FEARI} = \frac{\text{FEA Peak Wall Stress}}{\text{Experiment Wall Strenght}} \quad (4)$$

This basic index indicates the likelihood of failure by relating the stress acting on the AAA wall to the material strength.

Pulse Wave Imaging and Fluid–Structure Interaction Modeling

A pilot feasibility study using 3D-printed idealized AAA phantoms was conducted to determine suitability for ultrasound flow phantoms. Idealized models 3D-printed in HeartPrint material were chosen, based on the low UTS and favorable material selection criteria. The phantom was embedded in 6% gelatin to mimic tissue surrounding the vessel *in vivo*. A peristaltic pump circulated a pulsatile flow of water through the phantom. Radiofrequency signals were acquired using a Verasonics system (Verasonics Inc.) with a 2.5 MHz phased array transducer at a frame rate of 2,000 Hz with 128 beam lines. A fast, normalized 1D cross-correlation-based motion estimation method[33] was used on the radiofrequency signals to compute the incremental and axial displacements. The anterior and posterior walls were initially manually segmented, and temporal wall displacements were used to generate spatiotemporal maps of the anterior wall displacement waveform at each beam location. Further details on the experimental setup and procedure have been previously published.[19,33]

FSI simulations were carried out on the same geometry using the Coupled Eulerian-Lagrangian (CEL) solver in Abaqus/CAE. A free inflow boundary condition was applied to the tube inlet and a nonreflecting and zero-pressure boundary condition on the tube outlet; the neck and iliac legs were fixed. An initial fluid (water) velocity of 3.63m/s and a sinusoidal input velocity of 3.63m/s were applied, at a frequency of 5.4Hz on the tube inlet. Further details on the CEL method and the modeling parameters can be found elsewhere.[19,22,34,35]

Statistical Analysis

The Grubb's test was used to analyze the mechanical test data and identify the potential presence of outliers, based on a significance level of α=0.05. Sample means and standard deviations were calculated and tabulated.

Results

Uniaxial tensile testing revealed that the TangoPlus material compared favorably with the performance of the PDMS systems. HeartPrint Flex displayed a lower stress of 0.27MPa at failure, which is substantially lower than that of previously reported AAA tissue properties.[36] The 3D-printed TP material displayed the highest UTS variability, but this was comparable to S184. The addition of agar reduced the UTS of S184 closer to the other PDMS systems and AAA tissue.

The Sylgard series, according to Dow Corning product information sheets, have UTSs of 4.2, 2.4, and 6.7MPa, for S160, S170, and S184, respectively. Objet (now merged with Stratasys) reports the UTS for TangoPlus FLX930 as 1.5 MPa. Materialise reports the UTS of its proprietary material, HeartPrint Flex, as 500 kPa. Specimens were evaluated in the current study in as-cast and 3D -printed form, as it was deemed important to evaluate the material properties in as-processed form, which are likely to vary from specification sheet values obtained under ideal test conditions.

The tear propagation behavior was generally consistent with the typical material response of filled elastomer systems. Rather than relatively linear and steady tearing behavior, characteristic of unfilled systems, the tear paths tended to deviate in a saw-like manner, as the path curved around a filler particle and a new tear path initiated. This behavior was least pronounced in the case of S184, which would be expected as this elastomer is optically clear with reinforcing silica nanoparticle fillers.[37] The addition of agar microparticles significantly increased the tear strength of the S184 material. The tear strength of both 3D-printed materials was much higher than that of the investment-cast materials. It is important to note that the Sylgard materials are not specifically formulated for tear resistance. Presumably as interlayer delamination is a likely failure mode, 3D printing companies have attempted to mitigate this. Indeed, the manufacturers of HP material claim high flexibility and tear resistance; this is attributable to microparticle fillers (P. Verschueren, personal communication).

Multifrequency DMA testing revealed that the 3D-printed materials possessed durability equivalent to the investment-cast materials, under cyclic loading conditions up to 50 Hz. Visual inspection revealed no evidence of interlayer

MARY ANN LIEBERT, INC. • VOL. 1 NO. 1 • 2014 • DOI: 10.1089/3dp.2013.0010

delamination or failures at stress concentrations near the gripped regions. Both 3D-printed materials displayed similar dynamic tensile moduli, lower in comparison to the PDMS systems (Fig. 2). Mixing S160 and S170 resulted in a material with moduli closer to that of S170, at each frequency evaluated. The addition of agar to S184 increased the dynamic stiffness, closer to that of S170 and S160/170. The variability in dynamic stiffness properties of the mixed materials (S160/170 and S184A) was substantially higher compared with the other engineered materials.

Investment-cast and 3D-printed surfaces were visually inspected and examined at intermediate magnification using laser scanning confocal microscopy to investigate surface topography and quality (Fig. 3). The investment-cast materials consistently displayed the best surface finish, with average values for root mean square height of the surface (PSq) of 1.64 μm and arithmetical mean height of the surface (PSa) equal to 1.27 μm, respectively. Parallel sets of fine machining marks are observed to have transferred from the wax pattern to the PDMS internal surfaces, despite microgrit polishing of the aluminum molds. The PSq and Psa values were found to be 11 and 8.87 μm and 18.96 and 16.07 μm for the 3D-printed TP and HP materials, respectively. Compared with HP, TP displays a finer microstructure with a granular morphology, whereas the HP models display periodic peak and trough details. The 3D-printed layer thickness of the HP material is not known. For a more thorough discussion of areal surface texture parameters, the interested reader is directed to ISO 25178.

The finite element (FE) analyses for each of the model materials produced detailed von Mises stress distributions under physiological pressure loading of 120 mmHg, shown in Figure 4. Each material remained intact under loading; the peak wall stress and calculated FEARI results are shown in Table 1. The FEARI results for S170, S184A, and TP approach that of AAA tissue, under equivalent pressure. The 3D-printed HP material has a FEARI value of 0.96, indicating a low residual strength safety factor. Observation of the computed stress distributions reveals that regions of peak and elevated wall stress occur at inflection points rather than at regions of maximum diameter, which has been similarly reported in previous analysis of realistic AAA models.[11]

The results from the PWI and FSI simulations are shown in Figure 5, where the wall displacement magnitudes are displayed in chronological frames. Figure 5 illustrates the vertical (y) component of the wall displacement on the lower wall. Displacement corresponding to AAA lumen expansion is indicated by the arrows. In all frames, the early onset of displacements in the neck region of the aneurysm and subsequent wave propagation are visible.

PWI revealed that the wall motion in the straight segment closest to the inlet is relatively weak, which likely occurs because of the phantom being fixed at both ends by tube fittings. This subjects the phantom to boundary conditions unaccounted for in FSI simulations, which may be avoided by increasing the neck and leg lengths. At the onset of each pulse, the neck wall region of the idealized aneurysm experiences motion initially and relatively large displacements are evident. These regions correspond to the areas of peak aneurysm wall stress, indicated previously by FE analysis in Figure 4.

Three model types (idealized, patient-specific, and a healthy aorta) were initially sought to be produced by investment casting and 3D printing, utilizing a range of materials. All but the healthy aorta model were successfully reproduced, which proved near-impossible to produce phantoms of acceptable quality via investment casting (Supplementary Figure S2). Because of the model tortuosity and complex features such as the small-diameter iliac arteries and bifurcation, numerous air voids occurred. Efforts to eliminate voids by incorporating multiple injection and vent ports proved unsuccessful. Sagging of the wax pattern resulted in poor wall-thickness tolerances, despite utilizing alternative wax formulations and lead-based low-melt alloys. Typical investment-cast idealized AAA wall thickness variation has been reported as ranging between 4% and 11%,[10,26,38] increasing to 20–53% for the most complex patient-specific models.[38]

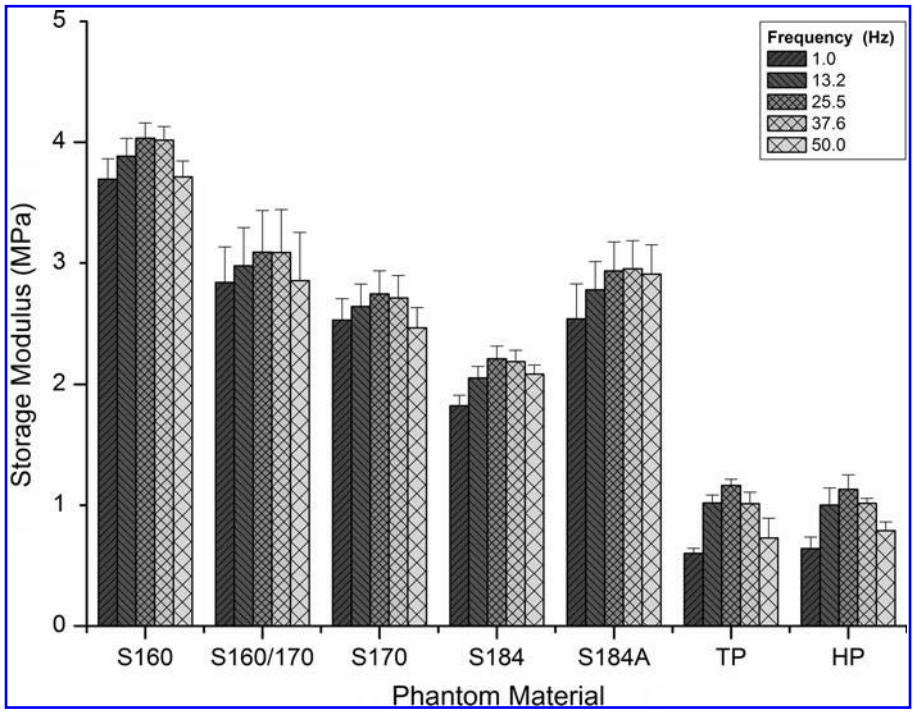

Figure 2. Storage modulus (E') for each phantom material as a function of frequency. HP, HeartPrint Flex; TP, TangoPlus FLX930.

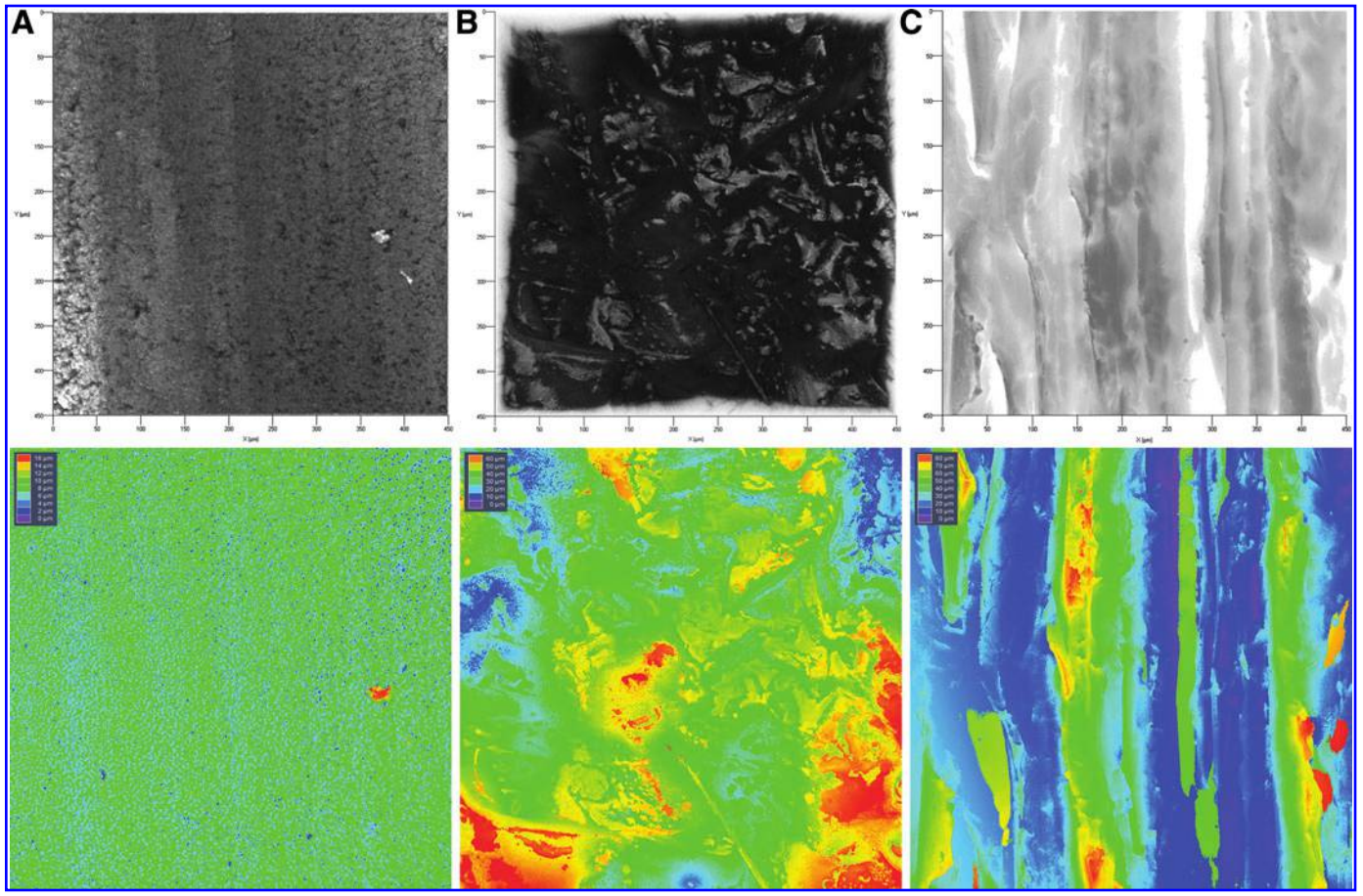

Figure 3. 3D topography and height maps are shown in the top and bottom rows, respectively, for selected phantom materials. Shown are **(A)** Sylgard 160, **(B)** TangoPlus FLX930, and **(C)** HeartPrint Flex. Note the residual machining marks in the case of Sylgard 160, typical of all models produced by the lost-wax casting process. Color images available online at www.liebertpub.com/3DP

Dimensional accuracy is greatly increased with the alternative use of the 3D printing process, being essentially governed by the print layer thickness. Although AAA wall thickness varies *in vivo*, it is important that wall thickness deviations be controlled for reliable imaging analysis and to prevent altering stress distributions.

Discussion

The objective of this article was to investigate the feasibility of 3D printing flexible vascular phantoms for computational validation and medical imaging applications. The 3D-printed materials displayed similar strength properties to PDMS elastomers and AAA tissue. Although less stiff under dynamic loading conditions, both materials remained intact postcyclical loading and displayed higher tear strengths compared with PDMS systems, indicating sufficient durability for short-term pulsatile flow applications and bench testing. The phantom surface finish was slightly inferior to investment-cast models, with a modest increase in surface roughness: only the HP material had clearly visible striations, presumably because of a higher print layer thickness. The textured surface finish may be improved by secondary processing operations (via coating, polishing, partial dissolution, etc.), which are beyond the scope of this study.

Of the materials evaluated, Sylgard 184/Agar, TangoPlus, and HeartPrint Flex possessed the most favorable material properties (especially translucency and scattering) for ultrasound phantom applications. Similar to native tissue *in vivo*, pulse wave propagation along the phantom wall was visualized with PWI. Regions of peak and elevated wall stress were shown to occur at inflection points rather than at regions of maximum diameter, which correlated well with the PWI finding that these were the regions where the largest displacements occurred. This has similarly reported in previous analysis of realistic AAA models[11] and will be the subject of future investigation using PWI and FSI. Assessment of arterial stiffness is being increasingly recommended as essential for clinical diagnosis and follow-up procedures,[39,40] and PWI shows excellent potential for routine implementation in the clinical environment.[17–23] Preliminary analysis with optical coherence tomography imaging indicates potential phantom applications also (data not shown), as light rather than sound is scattered.

The pathology of aneurysms is complex, consisting of the diseased artery wall with the frequent presence of soft intraluminal thrombus and hard

MARY ANN LIEBERT, INC. • VOL. 1 NO. 1 • 2014 • DOI: 10.1089/3dp.2013.0010

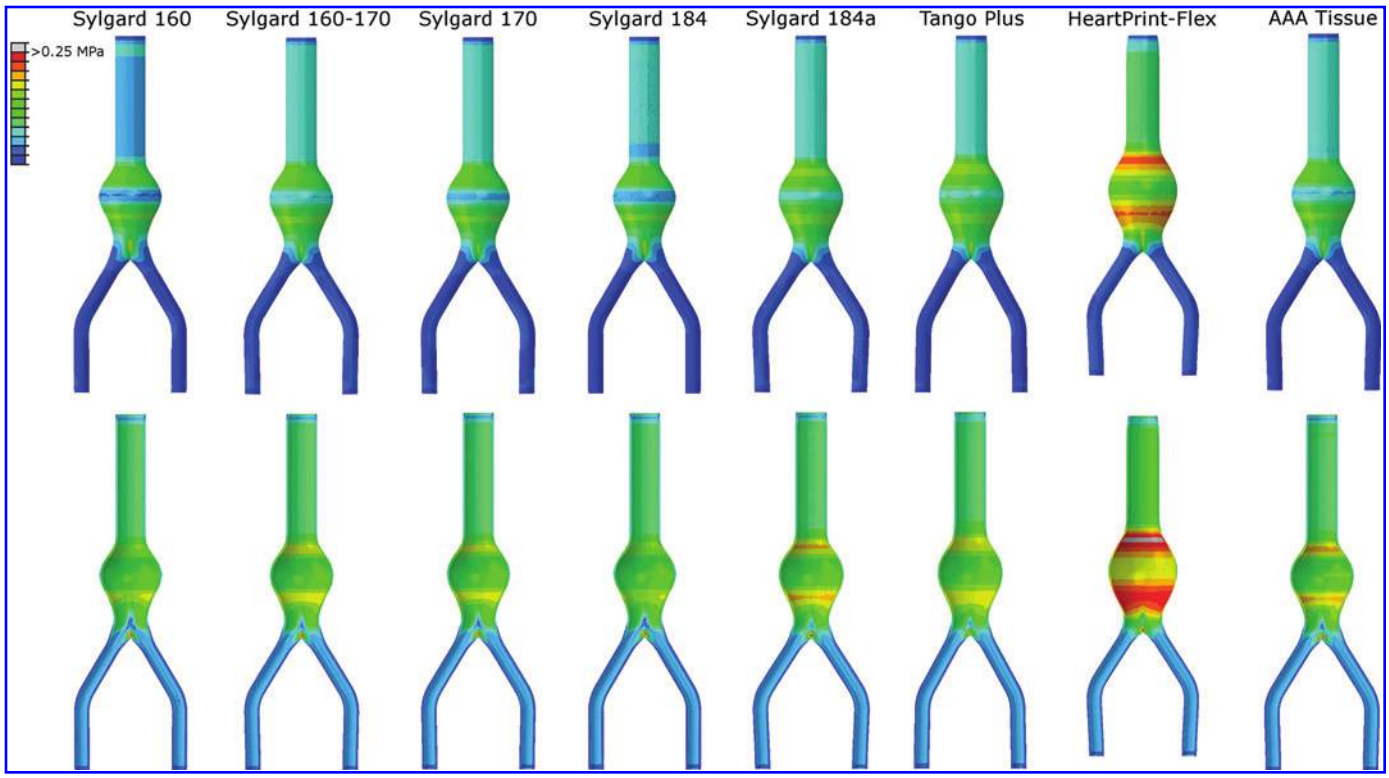

Figure 4. Computed stress distributions are illustrated for each material on the outer (top row) and inner (bottom row) surfaces for the idealized AAA model. Stress contours are normalized to 0.25MPa, approximately the peak wall stress of the HeartPrint Flex model. Color images available online at www.liebertpub.com/3DP

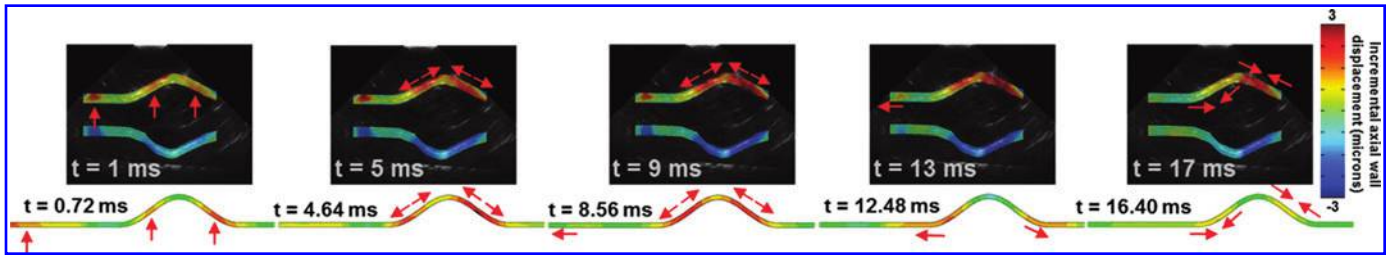

Figure 5. Time series showing the pulse propagation along the idealized HeartPrint Flex AAA phantom and resulting wall displacement magnitudes via PWI (top) and FSI simulations (bottom). Wall displacement corresponding to AAA lumen expansion is indicated by the arrows. FSI, fluid–structure interaction; PWI, pulse wave imaging. Color images available online at www.liebertpub.com/3DP

calcifications.[12,14,26,27,29,36,41,42] These components, coupled with variable geometry, wall thicknesses, anisotropy, and elasticity properties, result in complex wall stress distributions, making rupture prediction challenging. As multimaterial 3D printing is now possible, such as Objet's PolyJet technology, phantoms may be produced with regional material properties, incorporating some of these components. Recent advances in bioprinting, aiming to reproduce the structure and function of organs and tissues, present further possibilities for phantoms. Tunable mechanical[43,44] and porosity[45] properties, with cells incorporated in the primary[45,46] or a secondary deposited material,[43] have been demonstrated.

In summary, 3D-printed phantoms have great potential to improve computational modeling approaches, clinical imaging modalities, and medical device design and bench testing.[47–51] Physical models of complex anatomies may be employed to aid surgical consensus,[49,50] for outreach and education activities, and for the practice of surgical procedures.[48,51]

Conclusions

As a manufacturing process, 3D printing is well suited for the generation of biomedical phantoms, which is essentially a low-volume process for patient-specific models. The relatively high tooling costs for alternative processes such as lost-wax investment casting make 3D printing a cost-effective choice. Phantoms of complex geometry and tortuosity were successfully produced with superior dimensional tolerances. Such phantoms are likely to see increased

use in a diverse range of biomedical applications.

Acknowledgments

This work has been partially funded through NIH R01-HL098830. The SonixTOUCH ultrasound scanner was funded by the Irish Government's Programme for Research in Third Level Institutions, Cycle 5, National Development Plan 2007–2013, with the assistance of the European Regional Development fund. The Objet500 Connex 3D printer was funded through Grant 12/RI/2345(11) from Science Foundation Ireland. The authors would like to thank Dr. Áine Tierney and the technical staff of Department of Mechanical, Aeronautical and Biomedical Engineering at University of Limerick for valuable input in the creation of the idealized mold tooling, and Dr. Peter Verschueren at Materialise, Belgium, for valuable input regarding the HeartPrint Flex material.

Author Disclosure Statement

No competing financial interests exist.

References

1. Sakalihasan N, Limet R, Defawe OD. Abdominal aortic aneurysm. Lancet 2005;365:1577–1589.
2. Lederle FA. Ultrasonographic screening for abdominal aortic aneurysms. Ann Intern Med 2003;139:516–522.
3. Scott RAP, Bridgewater SG, Ashton HA. Randomized clinical trial of screening for abdominal aortic aneurysm in women. Br J Surg 2002;89:283–285.
4. Darling R, Messina C, Brewster D, et al. Autopsy study of unoperated abdominal aortic aneurysms. The case for early resection. Circulation 1977;56:II161–II164.
5. Limet R, Sakalihassan N, Albert A. Determination of the expansion rate and incidence of rupture of abdominal aortic aneurysms. J Vasc Surg 1991;14:540–548.
6. Mackiewicz Z, Molski S, Szpinda M, et al. Retroperitoneal rupture of abdominal aortic aneurysms. J Mal Vasc 1998;23:368–370.
7. Hak E, Balm R, Eikelboom BC, et al. Abdominal aortic aneurysm screening: an epidemiological point of view. Eur J Vasc Endovasc Surg 1996;11:270–278.
8. Thompson S, Ashton H, Gao L, et al. Screening men for abdominal aortic aneurysm: 10 year mortality and cost effectiveness results from the randomised Multicentre Aneurysm Screening Study. Br Med J 2009;338:b2307.
9. Ernst CB. Abdominal aortic aneurysm. N Engl J Med 1993;328:1167–1172.
10. Doyle BJ, Morris LG, Callanan A, et al. 3D reconstruction and manufacture of real abdominal aortic aneurysms: from CT scan to silicone model. J Biomech Eng 2008;130:034501.
11. Doyle BJ, Cloonan AJ, Walsh MT, et al. Identification of rupture locations in patient-specific abdominal aortic aneurysms using experimental and computational techniques. J Biomech 2010;43:1408–1416.
12. McGloughlin TM, Doyle BJ. New approaches to abdominal aortic aneurysm rupture risk assessment: engineering insights with clinical gain. Arterioscler Thromb Vasc Biol 2010;30:1687–1694.
13. McGloughlin T. Biomechanics and Mechanobiology of Aneurysms. Springer, Berlin, 2011.
14. Hoskins PR. Physical properties of tissues relevant to arterial ultrasound imaging and blood velocity measurement. Ultrasound Med Biol 2007;33:1527–1539.
15. Doyle BJ, Corbett TJ, Callanan A, et al. An experimental and numerical comparison of the rupture locations of an abdominal aortic aneurysm. J Endovasc Ther 2009;16:322–335.
16. Doyle BJ, Corbett TJ, Cloonan AJ, et al. Experimental modelling of aortic aneurysms: novel applications of silicone rubbers. Med Eng Phys 2009;31:1002–1012.
17. Vappou J, Luo J, Konofagou EE. Pulse wave imaging for noninvasive and quantitative measurement of arterial stiffness *in vivo*. Am J Hypertens 2010;23:393–398.
18. Konofagou E, Lee W-N, Luo J, et al. Physiologic cardiovascular strain and intrinsic wave imaging. Annu Rev Biomed Eng 2011;13:477–505.
19. Shahmirzadi D, Narayanan P, Li RX, et al. Mapping the longitudinal wall stiffness heterogeneities within intact canine aortas using Pulse Wave Imaging (PWI) *ex vivo*. J Biomech 2013;46:1866–1874.
20. Li RX, Luo J, Balaram SK, et al. Pulse wave imaging in normal, hypertensive and aneurysmal human aortas *in vivo*: a feasibility study. Phys Med Biol 2013;58:4549–4562.
21. Li RX, Qaqish WW, Shahmirzadi D, et al., Performance assessment and optimization of Pulse Wave Imaging (PWI) in *ex vivo* canine aortas and *in vivo* normal human arteries. Conference proceedings: Annual International Conference of the IEEE Engineering in Medicine and Biology Society 2012, pp. 3179–3182.
22. Shahmirzadi D, Li RX, Konofagou EE. Pulse-wave propagation in straight-geometry vessels for stiffness estimation: theory, simulations, phantoms and *in vitro* findings. J Biomech Eng 2012;134:114502.
23. Laheij R, Van Marrewijk C, Buth J. Progress Report on the Procedural and Follow up Results of 3413 Patients who Received Stent-Graft Treatment for Infra-Renal Abdominal Aortic Aneurysms for a Period of 6 Years. EUROSTAR Data Registry Centre 2001.
24. Morris L. Thesis: Numerical and experimental investigation of mechanical factors in the treatment of abdominal aortic aneurysms. University of Limerick, 2004.
25. Doyle BJ, Callanan A, McGloughlin TM. A comparison of modelling techniques for computing wall stress in abdominal aortic aneurysms. BioMed Eng OnLine 2007;6.
26. Corbett TJ, Doyle BJ, Callanan A, et al. Engineering silicone rubbers for *in vitro* studies: creating AAA models and ILT analogues with physiological properties. J Biomech Eng 2010;132:011008.
27. Raghavan ML, Vorp DA. Toward a biomechanical tool to evaluate rupture potential of abdominal aortic aneurysm: identification of a finite strain constitutive model and evaluation of its applicability. J Biomech 2000;33:475–482.
28. Fillinger MF, Marra SP, Raghavan ML, et al. Prediction of rupture risk in abdominal aortic aneurysm during observation: wall stress versus diameter. J Vasc Surg 2003;37:724–732.
29. Raghavan ML, Vorp DA, Federle MP, et al. Wall stress distribution on three-

dimensionally reconstructed models of human abdominal aortic aneurysm. J Vasc Surg 2000;31:760–769.
30. Doyle BJ, Callanan A, Walsh MT, et al. A finite element analysis rupture index (FEARI) as an additional tool for abdominal aortic aneurysm burst prediction. Vasc Dis Prev 2009;6:75–82.
31. Cloonan AJ, O'Donnell MR, Lee WT, et al. Spherical indentation of free-standing acellular extracellular matrix membranes. Acta Biomater 2012;8:262–273.
32. Menard KP. Dynamic Mechanical Analysis: A Practical Introduction. CRC Press, Boca Raton, FL, 2008.
33. Luo J, Konofagou E. A fast normalized cross-correlation calculation method for motion estimation. IEEE Trans Ultrason Ferroelectr Freq Control 2010;57:1347–1357.
34. Shahmirzadi D, Konofagou EE. Detection of aortic wall inclusion using regional pulse wave propagation and velocity. Artery Res 2012;6:3.
35. Shahmirzadi D, Konofagou EE. Quantification of arterial wall inhomogeneity size, distribution, and modulus contrast using FSI numerical pulse wave propagation. Artery Res 2014 [Epub ahead of print] DOI: 10.1016/j.artres.2014.01.006.
36. Raghavan ML, Kratzberg J, Castro de Tolosa EM, et al. Regional distribution of wall thickness and failure properties of human abdominal aortic aneurysm. J Biomech 2006;39:3010–3016.
37. Oláh A, Hillborg H, Vancso GJ. Hydrophobic recovery of UV/ozone treated poly(dimethylsiloxane): adhesion studies by contact mechanics and mechanism of surface modification. Appl Surf Sci 2005;239:410–423.
38. O'Brien T, Morris L, O'Donnell M, et al. Injection-moulded models of major and minor arteries: the variability of model wall thickness owing to casting technique. Proc Inst Mech Eng H 2005;219:381–386.
39. Laurent S, Cockcroft J, Van Bortel L, et al. Expert consensus document on arterial stiffness: methodological issues and clinical applications. Eur Heart J 2006;27:2588–2605.
40. Mancia G, De Backer G, Dominiczak A, et al., 2007 ESH-ESC practice guidelines for the management of arterial hypertension: ESH-ESC Task Force on the Management of Arterial Hypertension. J Hypertens 2007;25:1751–1762.
41. Maier A, Gee MW, Reeps C, et al. Impact of calcifications on patient-specific wall stress analysis of abdominal aortic aneurysms. Biomech Model Mechanobiol 2010;9:511–521.
42. Doyle BJ, Hoskins PR, McGloughlin TM. COMMENTARY: computational rupture prediction of AAAs: what needs to be done next? J Endovasc Ther 2011;18:226–229.
43. Schuurman W, Khristov V, Pot MW, et al. Bioprinting of hybrid tissue constructs with tailorable mechanical properties. Biofabrication 2011;3:021001.
44. Hockaday LA, Kang KH, Colangelo NW, et al. Rapid 3D printing of anatomically accurate and mechanically heterogeneous aortic valve hydrogel scaffolds. Biofabrication 2012;4:035005.
45. Fedorovich NE, Kuipers E, Gawlitta D, et al. Scaffold porosity and oxygenation of printed hydrogel constructs affect functionality of embedded osteogenic progenitors. Tissue Eng Part A 2011;17:2473–2486.
46. Cohen DL, Malone E, Lipson H, et al. Direct freeform fabrication of seeded hydrogels in arbitrary geometries. Tissue Eng 2006;12:1325–1335.
47. Biglino G, Verschueren P, Zegels R, et al. Rapid prototyping compliant arterial phantoms for *in-vitro* studies and device testing. J Cardiovasc Magn Reson 2013;15:2.
48. Sulaiman A, Boussel L, Taconnet F, et al. *In vitro* non-rigid life-size model of aortic arch aneurysm for endovascular prosthesis assessment. Eur J Cardiothorac Surg 2008;33:53–57.
49. Tam MD, Laycock SD, Brown JR, et al. 3D printing of an aortic aneurysm to facilitate decision making and device selection for endovascular aneurysm repair in complex neck anatomy. J Endovasc Ther 2013;20:863–867.
50. Sodian R, Schmauss D, Schmitz C, et al. 3-dimensional printing of models to create custom-made devices for coil embolization of an anastomotic leak after aortic arch replacement. Ann Thorac Surg 2009;88:974–978.
51. Baeck K, Lopes P, Verschueren P. 3rd Joint Workshop on New Technologies for Computer/Robot Assisted Surgery, Verona, Italy, 2013.

Address correspondence to:
Aidan J. Cloonan
MSG-013-031
Materials & Surface Science Institute
University of Limerick
Limerick
Ireland

E-mail: aidan.cloonan@ul.ie